Received 16 October 2022; revised 25 November 2022; accepted 4 December 2022. Date of publication 13 December 2022;
date of current version 23 January 2023.

Digital Object Identifier 10.1109/OJAP.2022.3228541

mmWave Yagi-Uda Element and Array on Liquid Crystal Polymer for 5G

RAJVEER S. BRAR (Graduate Student Member, IEEE), AND RODNEY G. VAUGHAN (Life Fellow, IEEE)

Sierra Wireless Mobile Communication Laboratory, School of Engineering Science, Simon Fraser University, Burnaby, BC V5A 1S6, Canada

CORRESPONDING AUTHOR: R. S. BRAR (e-mail: rsbrar@sfu.ca)

This work was supported by the Canadian Government Source: NSERC under Grant RGPIN-2022-05376.

ABSTRACT Arrays on personal terminals are feasible using mmWave frequencies, but are limited by mutual coupling. A standard specification for MIMO is −15 dB coupling which can be readily attained over a modest bandwidth, and decoupling modifications can reduce this to less than −20 dB. Such a change has relatively little impact on narrowband MIMO performance but is significant for wideband phased arrays, demonstrated here using simulation and measurement of a new design. For the element, we present a Yagi-Uda structure on PCB with a bandwidth from 22 to 44 GHz to cover a set of standard mmWave bands for 5G. Our prototype uses the RFIC packaging material Liquid Crystal Polymer which is suitable for Antenna-in-Package technology. For the array, the element spacing is set small enough to suppress grating lobes at the highest frequency. At the lowest frequencies, the lowest electrical spacing means the highest mutual coupling, and we apply a decoupling modification for this. The associated improvements in the impedance bandwidth, scan range, gain and radiation efficiency are presented for edge- and corner-mounted arrays designed for a mobile terminal such as a cellphone. Our array combining comprises simulation-based signal phasing and the simpler beam switching using element selection. The edge-mounted array has a 59% TARC bandwidth (24-44 GHz) over which the scan range is between ±60° and ±35°, the gain is 9.5 to 13 dBi with a radiation efficiency better than −0.2 dB. The corner-mounted switched array has peak gains of 6 to 9 dBi, showing the gain penalty associated with the simpler switched beam architecture. Finally, the impact of a cellphone chassis on the antenna performance is assessed by simulation.

INDEX TERMS mmWave antennas, array design, phased array, wideband, printed antenna, Yagi, LCP, 5G.

I. INTRODUCTION

THE FIFTH generation (5G) of wireless communications strives for new user experiences, higher throughput, lower latency, and higher spectral efficiency, e.g., [1], [2]. The main technique for improving performance is to use more antennas. This is enabled by the smaller wavelengths of mmWave frequencies - often interpreted as frequencies higher than 20 to 30 GHz - for array deployment on physically small terminals.

The Friis path gain of mmWave carriers is lower than that of the traditional lower frequencies. To maintain the SNR without transmitting higher power levels or consuming extra bandwidth, the antenna system must provide a higher effective gain, and the use of multiple antennas provides this. MIMO techniques can maximize the signal-to-noise-plus-interference ratio in multipath, whereas phased arrays maximize a geometric directive gain. Full MIMO (parallel channels of multiple data streams for each user) offers the best capacity efficiency in static conditions, but may not be feasible because of an excessive capacity overhead required for continual channel sounding of the fast-changing mmWave mobile channels, and because of its high complexity. Therefore, hybrid systems have been proposed, e.g., [3], that use the simpler phased array approach or the even simpler switched beam approach. Whether it's a switched beam, phased array, or MIMO system, the antenna performance is the critical factor. For the antenna design, the elements need to be wideband and have an efficiency as high as possible, and in the array, the mutual coupling must be low, with the question arising as to how low.

MIMO systems (for example, in the form of a chipset) typically call for at least −15 dB coupling between antenna

ports over a narrow relative bandwidth, e.g., [4], [5]. A reduction to well below −15 dB has relatively little impact on narrowband MIMO performance, but its impact on wideband phased array performance has not been studied. In terms of MIMO terminology, this decoupling can relate to making the element patterns "more orthogonal" over the propagation scenario [6].

In phased array terminology, the element patterns must be identical, and the physical spacing between elements becomes critical because, for wideband operation, there are opposing forces on the spacing from opposite ends of the band. At the highest frequencies, the elements have maximum electrical spacing with associated lower mutual coupling, but also must be sufficiently close-spaced to suppress grating lobes. At the lowest frequencies, the electrical spacing is the lowest and the associated higher mutual coupling causes gain loss and beam steering limitations. It is shown below that if the mutual coupling is more than −20 dB then the phased array's performance is affected. This happens at the lowest frequencies of a wideband array, and a solution is to deploy decoupling modifications.

Various types of antenna elements have been presented for mmwave frequencies. These range from slot loaded patches [7] and "fan" shaped patches [8] to cavity backed slots [9] and the wideband Yagi-Uda structures [10], [11]. Previous Yagi-Uda mmWave designs are: (i) a novel dual-polarization "quasi" Yagi-Uda structure that has the dipoles on the PCB with long vias through thick PCB substrate for radiating the other polarization, with a 25% impedance bandwidth centered at 25.5 GHz [12]; and (ii) a more conventional single-polarization Yagi-Uda array [13] with 18% impedance bandwidth at 27.5 GHz. A common feature in these and other previously presented antennas or arrays [7], [8], [9], [10], [11], [12], [13], [14], [15], [16], [17], [18] is that they do not have sufficient bandwidth to support the set of 3GPP-tagged 5G mmWave frequency bands (24.25-27.5, 26.5-29.5, 27.7-28.35, 37-40, 39.5-43.5 GHz).

Our designs are realized on printed circuit board (PCB) in order to make them inexpensive, e.g., [6], and use RFIC packaging material Liquid Crystal Polymer (LCP) which is suitable for Antenna-in-Package (AiP) technology [19], [20], [21]. The LCP manufacturer claims [22] that the advantages of LCP over traditional dielectric materials, i.e., various FR4s, Rogers substrates, ceramics, etc., include: lower dissipation at mmwave frequencies; low moisture absorption; low thermal expansion, more mechanical flexibility, and lower cost.

Our LCP based Yagi-Uda element attains the goal of covering the current 3GPP mmWave bands given above. The various results plotted below go outside these bandwidth limits, as per good practice for device design. Another design goal is to strive for the same wide bandwidth for the array. Previously presented arrays do not discuss array design for such wide bandwidths, where mutual coupling issues come to the fore. We present a new design methodology for these wide bandwidths.

Regarding handset born arrays, an important example is [23], which presents a beam switching array on a mobile phone chassis. Their Yagi-Uda type elements are different from each other, and have a comparable bandwidth to the element presented in this paper. Two-beam switched arrays are presented in [17] and [18], demonstrating their feasibility when mounted on the long edge of a chassis. These prior works seek to configure mmWave arrays on mobile terminals for full spherical coverage and in the absence of a user. To the best of the authors' knowledge, there is no prior treatment on the impact of chassis integration relative to the stand-alone operation of mmWave arrays.

The new contributions of this paper are as follows. A wideband element on PCB is presented, and a new wideband array design approach guides the choice of the element spacing at the highest frequency. The traditional formulation for a given scan range results in the elements being unnecessarily close, which impacts the lowest frequency behaviour of a wideband system because of the mutual coupling. Our approach instead uses a simple element pattern model in the array directivity function to guide the element spacing. For the same scan range, our approach results in a wider bandwidth than existing mmWave phased array designs. Also, we present new numerical analysis of the mutual coupling and the effects of a groundplane on the array gain and on the bias of the realized beam direction relative the beam steering vector direction. Finally, we include new results on the integration of our Yagi-Uda elements as AiPs, mounted within a metallic chassis.

Section II discusses antenna element design using simulation (CST) and measurements of prototypes. Section III is an investigation of beam forming by phased array, mutual coupling affects, and a corporate feed. Section IV presents a switched element antenna system. Studies on integrating the antenna system inside a cellphone chassis are given in Section V, and Section VI concludes the paper. An Appendix compares the performance of the presented design with previously published designs.

II. ELEMENT DESIGN

The element design is given in Fig. 1. The PCB comprises 4 layers of 4-mil LCP dielectric, adhered by a 1-mil layer of bonding sheet (FL-A3000) [24]. The 4 layers provide the substrate thickness needed for the wide bandwidth, and the conductor is on the outer surfaces only. The relative dielectric constant of LCP is specified as 3 with a loss tangent of 0.0016, at 10 GHz [25], and this is the basis for our simulations despite the unknown values for the adhesive layers. At the back of the Yagi-Uda element, there is a stitched-via wall to suppress propagation to the PCB. The through-hole vias have a diameter of 10 mil and the pad diameter is 15 mil. The via pad is wider than the hole by 2 mil to allow for laser drill movement tolerance. At mmWave frequencies, filled copper vias and through-hole vias have similar RF performance because of the skin effect. (The skin depth at 28 GHz for copper plated vias is around

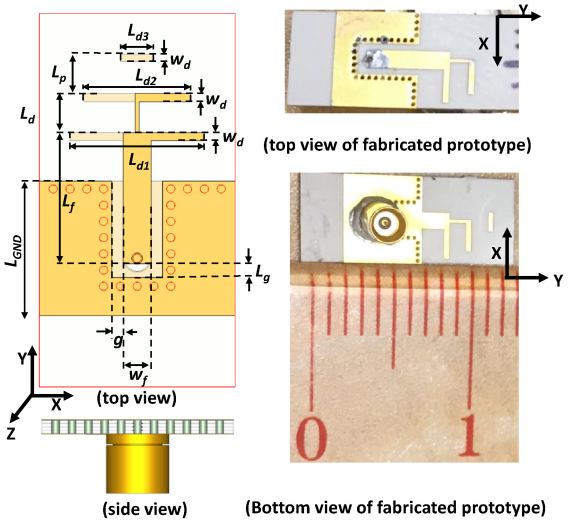

FIGURE 1. Yagi-Uda element on two-sided PCB. The fabricated prototype size is 5 mm by 13 mm. [$W_f = 1$, $W_d = 0.3$, $L_{GND} = 4.8$, $L_g = 0.5$, $L_f = 4.7$, $L_d = 1.4$, $L_p = 1.4$, $L_{d1} = 4.8$, $L_{d2} = 3.8$, $L_{d3} = 1.2$, $g = 0.42$]. (Units in mm).

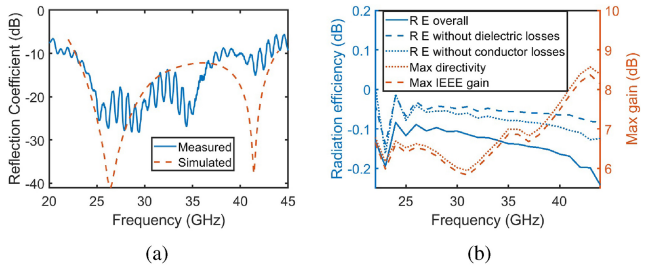

FIGURE 2. (a) Simulated and measured reflection coefficients, and (b) simulated gain and radiation efficiency (RE) of our Yagi-Uda element.

0.015 mil (0.39 µm) while the plating thickness of via is 1 mil.)

For a printed Yagi-Uda element, the substrate thickness is often kept as thin as possible in order to avoid cross polar radiation from the feed lines and vias. In mobile channels, polarization purity is seldom required because the multipath mixes the polarizations, and the physical orientation of the handset is somewhat random. So in a classical mobile scenario model (uniform, uncorrelated, equal polarizations), the polarization efficiency of any single-port antenna is one half because of the mixed polarization. When there is a dominant line-of-sight situation (classical point-to-point) the polarization becomes important. Most mmWave channels, such as small (femto-) cell and other indoor links, are likely to be dominantly line-of-sight situations.

Fig. 2(a) shows a −10 dB impedance match from 22.8 to 44 GHz, where the wide bandwidth is from the PCB fabricated parallel connection of two different length dipoles [24], [26]. There is reasonable agreement between the measured and simulated impedance bandwidths, except at the higher frequencies where the measurements become challenging. The regular ripple in the measurements is from reflections at the limited-life push-on mmWave connectors.

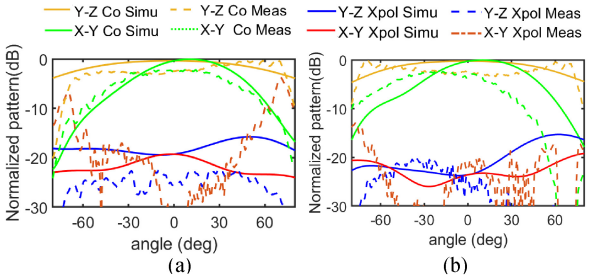

FIGURE 3. Normalized, measured and simulated patterns of our Yagi-Uda element at (a) 25 GHz (b) 28 GHz. The measured peak gain at 25 GHz is 6.8 dBi and at 28 GHz is 6.5 dBi, as compared to simulated realized gains of 6.5 dBi and 6 dBi, respectively.

These become mismatched after a few uses. This ripple can be easily removed by averaging but we present raw measurement data in this paper.

Fig. 2(b) shows the simulated radiation efficiency to be −0.1 to −0.2 dB. It is currently not feasible to measure high radiation efficiency accurately. (This requires full pattern mmWave measurements where the gain, even in its maximum direction, can seldom be estimated to better that ± 0.5 dB.)

Fig. 3 shows samples of element pattern cuts for the E-plane (x-y), and H-plane (y-z). The simulated 3 dB E-plane beamwidths are 63°, 66°, at 25 GHz and 28 GHz respectively, and for the H-plane, 140° and 135°. Measuring patterns at these frequencies is challenging, including just the alignment of such a physically tiny element. There is reasonable similarity between the simulated and measured patterns, including the cross polar level. More on the measurement setup is given in Section III.

III. WIDEBAND ARRAY ANTENNA

Many array results, particularly relating to mutual coupling, stem from "infinite" array theory. Such classical approaches assume separable array and element factors (patterns) which is an insightful model for the array mechanism. But on a finite platform, the assumption of array and element factorization, or the associated separation of the array and element directivities, do not hold. Nevertheless, infinite array considerations are still used for design guidelines.

A. ELEMENT SPACING DESIGN

The maximum element spacing is traditionally chosen using the "no grating lobes" condition from the array factor. For a beam steered to angle θ_S off broadside, this spacing is, e.g., [27],

$$d_{max} = \frac{\lambda}{1 + sin(|\theta_S|)}. \quad (1)$$

The element pattern also affects the spacing choice, and a standard approach is to accept some grating lobe presence and suppress it using directive elements. Here we instead find the spacing from estimating the 3 dB scan range from the array antenna directivity (i.e., including the element patterns). For this, a simple main-lobe pattern

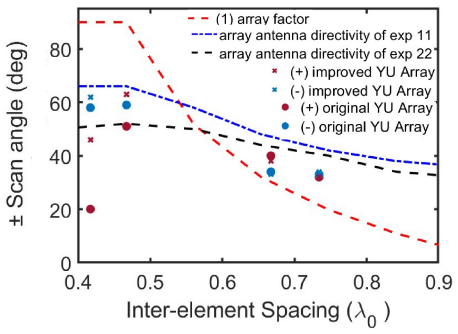

FIGURE 4. Scan range against element spacing for a 4-element array with the element pattern as a parameter. The array factor represents isotropic elements, and the other element directivities are modelled for hemispheric coverage (infinite ground-plane) and no mutual coupling. The figure shows how the scan range decreases for larger spacing and for more directive elements. Directivities for exp 11 and exp 22 are 7.8 dBi and 10 dBi. We use a $0.75\lambda_0$ spacing at 44 GHz (= 5 mm).

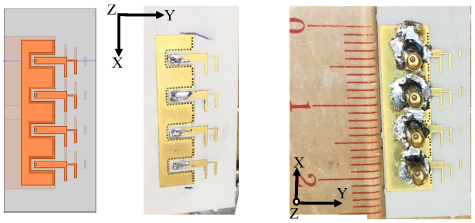

FIGURE 5. The prototype array of a 4 element Yagi-Uda antennas. Left and middle: the PCB layout. Right: showing the press-fit coaxial connectors to the elements.

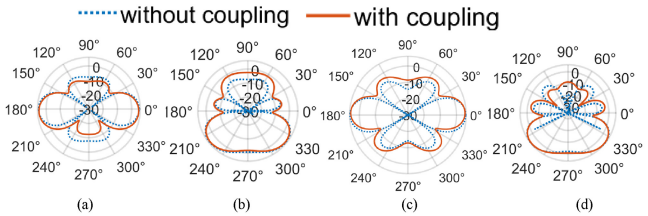

FIGURE 6. Array factor pattern cuts (*x-y* plane) in dBi for 4 sources placed along *Y* axis, array broadside at 0°, with and without mutual coupling at (a) 25 GHz broadside (b) 25 GHz for beam scanned to −45° (c) 28 GHz broadside (d) 28 GHz for beam scanned to −45°. The mutual coupling causes a gain reduction through loss as well as through directivity reduction from pattern changes.

model, $h(\theta, \phi) = cos^{2n}\theta cos^{2m}\phi$, is used, which is referred to as "exp nm". The best integer fit for our element patterns is exp 11 with hemispherical directivity 7.8 dBi and beamwidth 90°.

Fig. 4 presents some 3 dB scan ranges against the spacing, calculated from the array factor approach and from the array antenna pattern approach using modelled directive element patterns. It is seen that for spacings greater than $0.6\lambda_0$, the array antenna approach yields a larger scan range than the array factor approach. In particular, the array antenna directivity for exp 11 shows a 3 dB scan range of 45° for an element spacing of $0.75\lambda_0$. Following this, we chose a 5 mm spacing corresponding to $0.75\,\lambda_0$ at 44 GHz. When using the Yagi-Uda element, the 3 dB scan range (discrete markers in the figure) is seen to be asymmetric relative to broadside, and this is caused by the asymmetric structure of the PCB implementation of the elements.

The figure also includes results for the improved design used for studying the impact of reducing the mutual coupling on the phased array performance. (The design modification [28] is described in Fig. 8 below.) For wideband antennas, the mutual coupling naturally reduces at the higher frequencies in the operating band due to the increase in the electrical spacing between elements. The "improved" design is seen to have a larger scan range than the "original" design due to its reduced mutual coupling at the lower frequencies from the modification. There is no change for the higher frequencies such as 44 GHz, because here the mutual coupling is already below −25 dB, and it turns out that this level is low enough to not have significant impact on phased array performance.

B. MUTUAL COUPLING AND SCAN RANGE

The Pozar model is for including the impact of mutual coupling in the array antenna directivity. It uses the array factor with an isolated element pattern [29], or in a revised model [30], an embedded element pattern of a central element of a large array. These models (equations not included here) contain the S-parameters which bear the mutual coupling information.

Fig. 5 shows the simulated and prototype "original" array antenna. We use the S-parameter matrices from these structures in the Pozar model to look for any systematic impact of the mutual coupling on the array pattern.

Fig. 6 (a) to (d) are the 4-element array antenna's pattern cuts from using the Pozar model, for the conditions given in the caption. The pair of plots on each graph are *with* and *without* the mutual coupling. For *without*, we set the off-diagonal S-parameters to zero.

For 25 GHz, the broadside beam and scan direction −45° are in Fig. 6(a) and (b). The mutual coupling is seen to slightly broaden the main lobe at broadside, and lower the (single) side lobes at ±90° by some 3 dB. But when the beam is steered to 45°, the mutual coupling causes the side lobes to increase by about 4 dB. These results show that little can be concluded regarding systematic impact of the mutual coupling on the array pattern. This is because of the multiple mechanisms of these pattern changes. For example, for an element spacing of $0.42\lambda_0$ (25GHz), the adjacent element coupling phase is about +125° (not shown), and from the array factor associated with this phase progression, we may expect to see a contribution to the pattern from the mutual coupling in the direction of 56° (and 124°) from the main lobe. In any event, the peak gain of a phased array is reduced by the mutual coupling in two ways - increased loss through the coupled element energy being absorbed in the loads of the other the elements, and changes in the patterns (often higher sidelobes) causing a change of directivity.

At 28 GHz, the changing sidelobe level is still significant, as can be seen for broadside pattern of Fig. 6(c). But for the highest frequencies (not shown), we have $|S_{ij}| < -25$ dB,

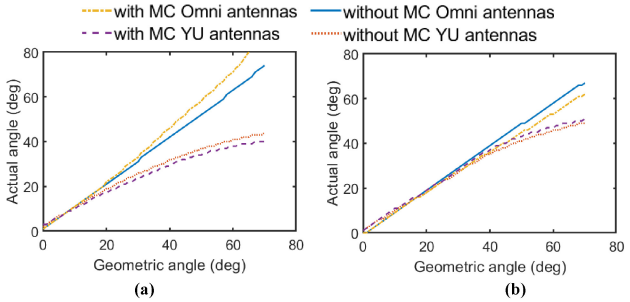

FIGURE 7. The bias in the beam steering direction due to mutual coupling, (a) at 25 GHz, (b) at 28 GHz. The bias direction depends on the sign of the phase (not shown here) of the mutual coupling.

and this level of mutual coupling has a negligible effect on main lobe, including its gain.

C. STEERING ANGLE BIAS

The mutual coupling causes the maximum gain direction to be biased from the expected geometric steering angle. This is shown in Fig. 7, where the cases are: with and without the mutual coupling; omni elements and our Yagi-Uda elements. The bias is larger for the lower frequencies where the mutual coupling is larger. For the results of the Yagi-Uda element in Fig. 7, the Pozar formulation was not used because it does not account for small arrays. The array antenna pattern was instead found from the array pattern formulation in [31] which contains the S-parameters and the embedded element patterns (simulated) with the *remaining elements open circuited*. (We have found this more recent formulation to be accurate [32].) For the *without mutual coupling* case in Fig. 7, the off-diagonal S-parameters are set to zero in this formulation. Finally, the opposing bias directions at 25 GHz and 28 GHz is from opposing phase signs in the mutual coupling (expressed as either Z_{ij} or S_{ij}) at these frequencies.

D. BANDWIDTH

Fig. 8 shows (a) the decoupling modification, and (b)-(d) the improvement of the array antenna bandwidth for the improved design. For 25 GHz and 28 GHz, the improved design has S_{21} at about -20 dB and -25 dB respectively, i.e., lower than the original design by about 10 dB. The active reflection coefficients were calculated using a phased-array formulation from [29] which contains the steering angle and element locations. From Fig. 8(c), the active reflection coefficients remain below -10 dB where the transmission coefficients (off-diagonal elements of S-parameter matrix) are lower than -20 dB. All ports of the original design have a -10 dB active reflection coefficient bandwidth of 29 to 44 GHz. The improved design has its low frequency performance extended to have an active reflection coefficient bandwidth of 24 to 44 GHz.

In Fig. 8(d), the total active reflection coefficient bandwidth (TARC) [5], [33] compares the array bandwidths of the original and improved designs for when the beam is steered to 30° and 45°. These results confirm the array bandwidth

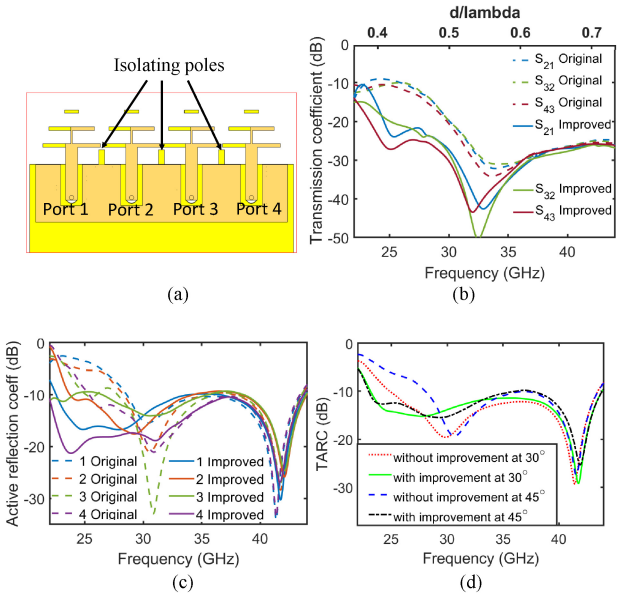

FIGURE 8. (a) The decoupling modification is printed "poles" of length $\lambda_g/8$ (guided wavelength), ≈ 1mm at 25 GHz. Their width is relatively insensitive, and we use 0.5 mm. (b)-(d): The port impact by simulation: the transmission (S-parameter) coefficients between adjacent elements; the active reflection coefficients for the beam steered to 45°; and the TARC comparison between the original and the improved designs.

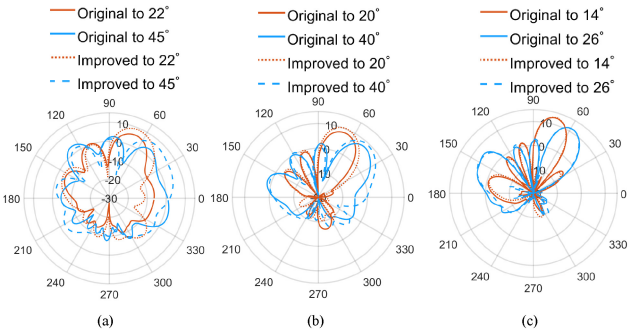

FIGURE 9. Beam steering cases (Broadside = 90°) for the 4-element array at (a) 25 GHz (b) 28 GHz (c) 40 GHz. At 25 GHz, the element spacing is 0.4 λ_0, and the scan range is limited by mutual coupling; whereas at 40 GHz, the scan range is unaffected because the coupling is low.

improvement from the reduced mutual coupling, in terms of the TARC metric.

The critical reduction in the mutual coupling from between -10 and -15 dB, to less than about -20 dB, improves not only the scan range and TARC bandwidth, shown above, but also the array antenna gain and radiation efficiency, shown below.

E. GAIN

Computer signal combination is used to combine the array elements. Some beam formed patterns are presented in Fig. 9 for the original and improved designs, with key results in Table 1. The improvements at 25 and 28 GHz are clear, and at 40 GHz the patterns are the same, as expected.

An ideal 4-port array (identical element patterns, no mutual coupling) should have 6 dB array gain. But a small,

TABLE 1. Peak gain and scan range comparison of original and improved.

Freq	Original		Improved	
-	Gain	Scan range	Gain	Scan range
GHz	dBi	3dB	dBi	3dB
25	8.96	+20° to -55°	9.8	+45° to -60°
28	9.8	+45° to -60°	10.4	+62° to -60°
40	12.96	40° to -35°	12.96	40° to -35°
44	13.7	35° to -35°	13.6	35° to -35°

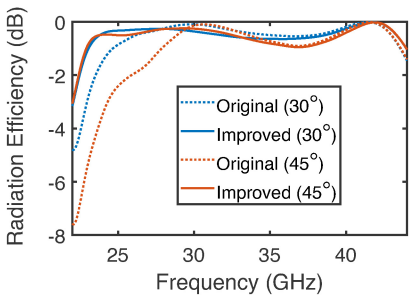

FIGURE 10. Simulated radiation efficiency for the two critically different mutual coupling levels at low frequencies, and different beam steering angles. The radiation efficiency drops as the beam is steered further from broadside due to increased mutual coupling.

complex platform will not support the identical element patterns assumed for this gain. Here, we co-phased the embedded element patterns at broadside before adding, and compared the resulting gain with the dB average of the embedded elements. This gives array gains for the original (improved) design of 3.6 dB (4.5 dB) at 25 GHz, 3.7 dB (4.3 dB) at 28 GHz, and 5.1 dB (5.1 dB) at 40 GHz. The shortfall of array gain is not just because the mutual coupling invokes extra loss, but also because the dissimilar element patterns reduce the expected (from an ideal array) directivity.

It is noted that for dissimilar element patterns, maximum ratio combining (as opposed to the equal gain combining of a phased array) would give the maximum gain possible for any defined direction. This beam forming would require look-up tables based on knowledge of the embedded element patterns for the weights, a topic for future work.

Fig. 10 shows the radiation efficiency of the ideal equal gain combining of a phased array against frequency, with some scan angles as a parameter. The difference in the antenna efficiencies between the original and improved designs is due to the changed mutual coupling.

From Table 1, the improved design has its broadside gain improved by 0.8 dB and 0.6 dB at 25 GHz and 28 GHz respectively. These values are greater than the change in the radiation efficiency, so there is apparently some change in the pattern directivity as well, and this is consistent with a change in coupling relating to a change in the correlation between the patterns, e.g., [6].

F. CORPORATE FEED FOR FIXED BEAM

Fig. 11 shows the array antenna prototypes with and without a corporate feed network. This fixed feed gives a fixed beam

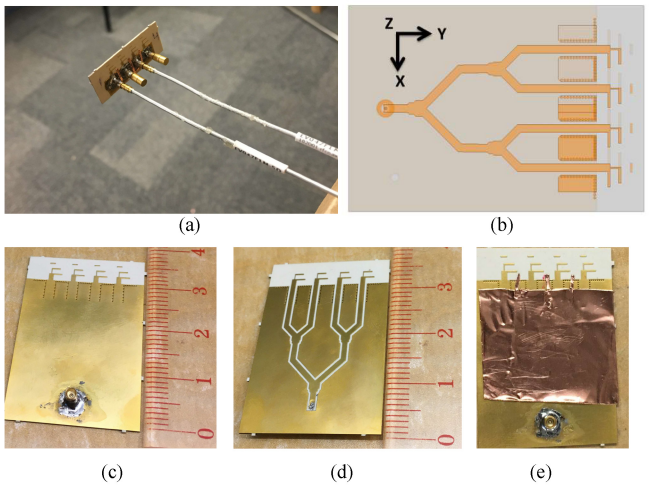

FIGURE 11. Corporate fed array: (a) port test configuration on a small ground-plane, using a 2-port VNA with the other two ports terminated. (b) Corporate feed version: (c-d) bottom and top views of prototype; (e) bottom view with hand made copper tape decoupling modification.

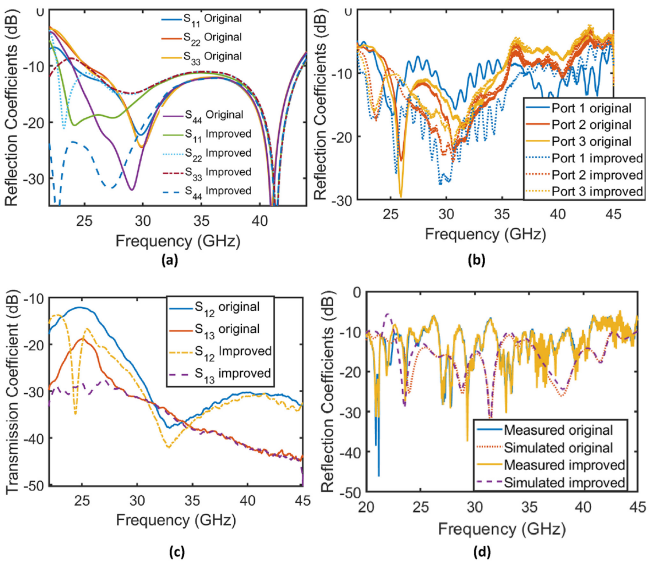

FIGURE 12. (a) Simulated and (b) measured reflection coefficients of discretely fed antenna elements on a minimal groundplane; (c) measured transmission coefficients at the discrete ports; (d) measured reflection coefficient at the single-port of the corporate feed (shown in Fig. 11).

and is only to check array functionality. We note that the size of a corporate feed tends to be much larger than the array, so where size is a critical resource, such as on a handset, such feeds are not likely to be feasible.

For testing at the ports of the elements, a Keysight Field Fox VNA was used with the unconnected ports having G3PO standard 50 Ω terminations, see Fig. 11(a). (For testing the corporate feed port, only a single-port measurement is required.)

Fig. 12 shows (a) simulated and (b) measured reflection coefficients at the 4 ports (i.e., no corporate feed) for the original and improved design on a minimal ground-plane. The regular ripple in the raw measurement data is again

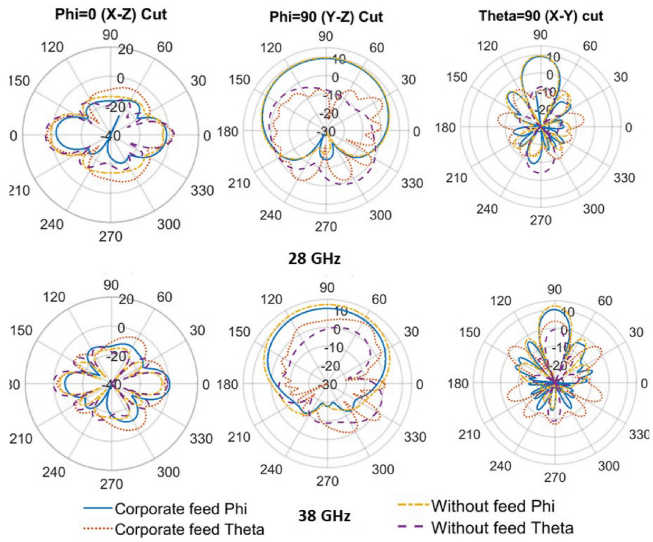

FIGURE 13. Simulated gain patterns (dBi) of the 4-element array, with and without the corporate feed, demonstrating the array action. Broadside is at 90°. The losses within the corporate feed reduce the gain of the array (relative to an ideal array) by up to 2 dB around the upper frequencies. Also, the corporate feed structure contributes cross polarization at higher frequencies.

caused by mismatch at the connector, and could be averaged out. Although the simulated and measured data, (a) and (b), do not match very well - see especially above 40 GHz, both indicate that the reduced mutual coupling of the modified design improves the match.

Fig. 12(c) is the measured coupling between the discrete ports (i.e., no corporate feed), showing the decrease for the improved design at the low frequencies. Fig. 12(d) shows the simulated and measured single port impedance bandwidths for the corporate fed array. Recall that the frequency range on the plot well exceeds the bandwidth we are seeking, which is 24.25-43.5 GHz. The results for original and improved designs show no significant difference, because: (i) the mutual coupling improvements are less pronounced for the broadside radiation of a corporate fed array and (ii) at any frequency, the corporate feed port match is essentially the same overall level as when it has matched terminations instead of the elements (not shown). Finally, the measured reflections are somewhat higher that the simulated ones. This is also the case in the prior mmWave Yagi-Uda array paper [23]. The measured bandwidth must be couched as a −5 dB match, rather than a −10 dB match. It is noted in passing that when a user is present, cell-phone antennas tend to have a better match because some of the transmitted power is absorbed is in the users' hand or head, and this manifests as a better impedance bandwidth at the feed. In any event, the corporate feed array study confirms reasonable impedance bandwidth of the antenna when it's operating as an array.

Fig. 13 presents simulated pattern cut examples for the discretely excited array with computer combining, and for the corporate fed array, demonstrating the array action, for (Top:) 28 GHz and (Bottom:) 38 GHz. At 28 GHz, using

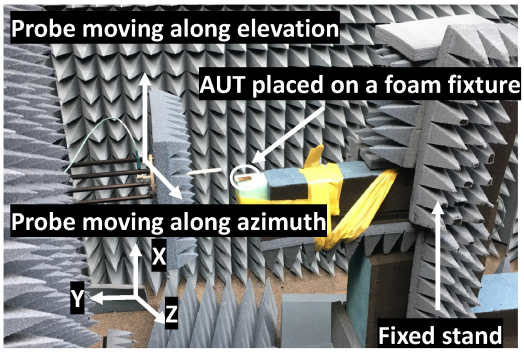

FIGURE 14. Pattern measurement set-up with an NSI system.

the corporate feed does not appreciably reduce the peak gain (from 9.6 to 9.5 dBi), and the cross polar gain in the main lobe remains at about −8 dBi for both cases. At 38 GHz, the peak gain reduces from 12.1 to 10.1 dBi due to a higher loss in the corporate feed at this frequency. Also, the cross polarization level in the main lobe increases significantly (from −0.74 to 3.87 dBi) due to radiation from the electrically thicker corporate feed structure.

G. PATTERN MEASUREMENT

Mostly, mmWave systems are tested using Over-The-Air systems which cannot separate, say, the antenna performance from the signal-processing performance. However, the patterns are critical parameters for phased arrays.

As noted in Section II, pattern measurement is very challenging at mmWave frequencies, and the full set of directions cannot be rendered due to the finite near-field aperture. The pattern measurement set-up for the corporate-fed array in our NSI near field chamber is shown in Fig. 14.

For such a wideband measurement, different probes are required for different parts of the band. For 24-33 GHz, a WR34 probe is used with a calibration standard gain horn (SGH34). For 33-40 GHz, the combination is WR22 and SGH22. The IF bandwidth can be controlled and offers a trade-off between manageable measurement time and measurement accuracy. For 24-33 GHz, we used 3 kHz, and for 33-40 GHz, the higher losses in the measurement system meant that we needed to use 300 Hz (and an extremely long measurement time - several days).

Fig. 15 shows pattern cut examples (25, 28, and 38 GHz), by simulation and measurement for the corporate fed array and these match reasonably well including the cross polarization levels. In summary, the measured gains are 8.5 dBi, 10 dBi and 11.8 dBi respectively, while the simulated gains are 9 dBi, 9.5 dBi and 10.1 dBi; so differences of about (0.5 dB, 0.5 dB, and 1.7 dB) at (25 GHz, 28 GHz, and 38 GHz). The improved design has a gain increase of 0.5 dB at 25 GHz and 0.3 dB at 28 GHz, in both simulation and measurement (not shown.) The corporate fed array pattern behaviour confirms the 4 elements are functioning as an array over the bandwidth.

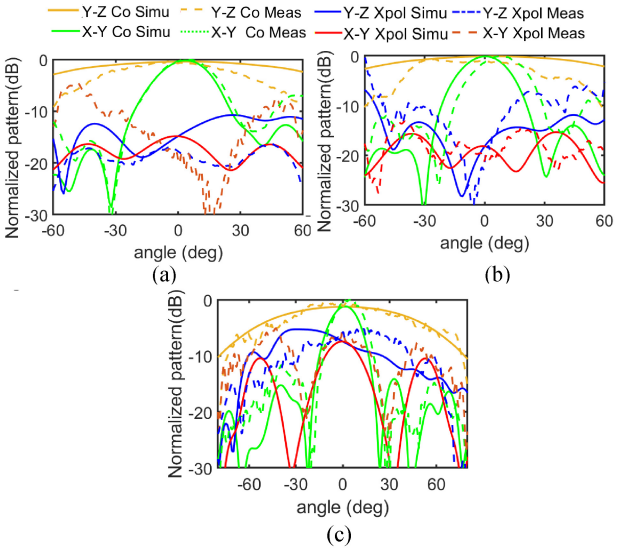

FIGURE 15. Measured pattern of 4 element array (original) with corporate feed network at (a) 25 GHz, (b) 28 GHz, (c) 38 GHz. The measured gains at these frequencies are 8.5 dBi, 10 dBi and 11.8 dBi respectively.

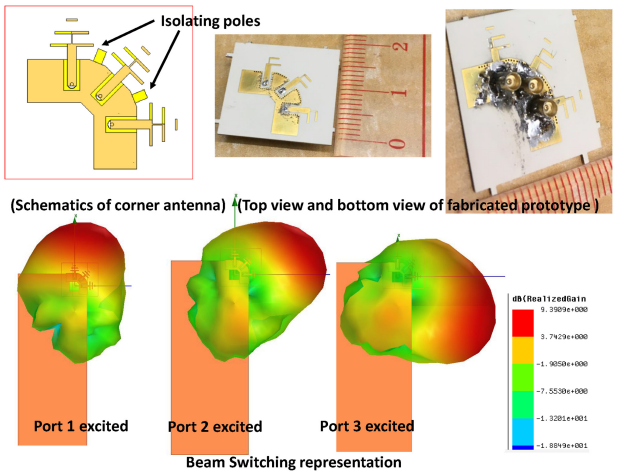

FIGURE 16. Schematics of corner beam switching antenna with fabricated prototype, and simulated pattern depiction.

IV. SWITCHING COMBINATION: ARC SHAPED ARRAY

Beam switching offers a simpler beamforming architecture compared to a wideband phased array system, especially for a large scan range. Its disadvantage is not harnessing the power of an array which is to use all the elements simultaneously. (To compensate, the elements used in beam switching can be different from each other and have a higher gain than those of a phased array, with the patterns and number of elements arranged for a coverage requirement, e.g., [23].) Here we use the same Yagi-Uda elements as above, arranged as a three element array on an arc, shown in Fig. 16 with depicted patterns. While an advantage of switched combining is the removal of mutual coupling (by setting the unused elements to open circuit - so there are no feed currents for these elements), we keep the unused elements loaded rather than open circuit to include the impact of mutual coupling within this configuration.

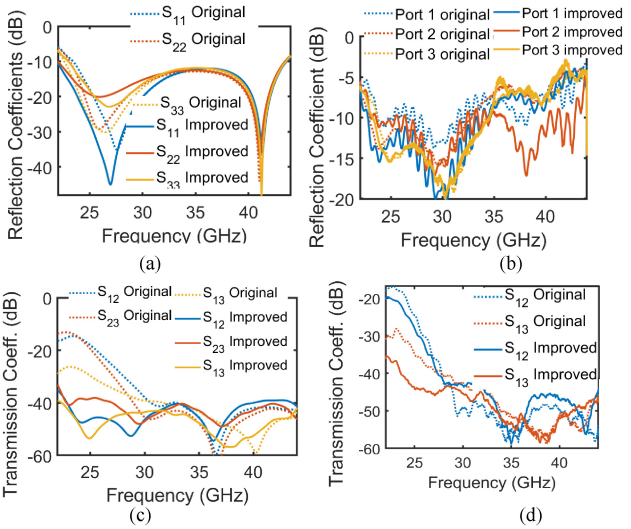

FIGURE 17. Scattering parameters for the arc shaped array. (a) simulated reflection coefficients, (b) measured reflection coefficients, (c) simulated transmission coefficients, and (d) measured transmission coefficients. The decoupling modification again decreases the coupling between antenna ports at lower frequencies, to be lower than −35 dB throughout the operating bandwidth.

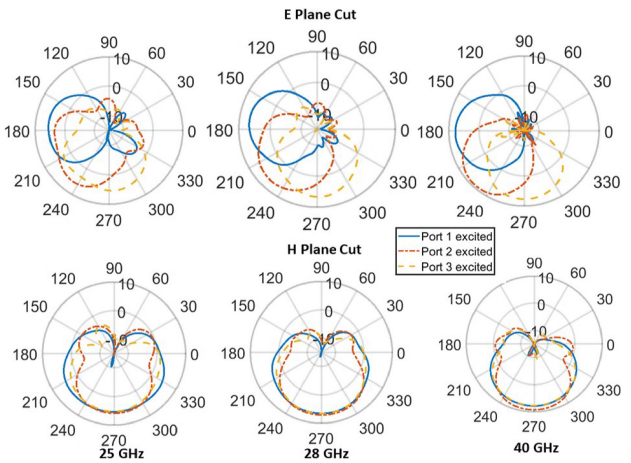

FIGURE 18. Simulated patterns of the beam switched configuration for the original design at 25, 28 and 40 GHz. The nominal beam directions are 180°, 215°, and 270°.

Fig. 17 gives the simulated and measured S-parameters for the original and improved designs for the *unused elements terminated*. As with the linear array, the decoupling modification improves the simulated impedance bandwidth of all the ports by 2-3 GHz to be: 22 to 43.5 GHz for ports 1 and 2, and 22.3 to 43.5 GHz for port 3. The measured transmission coefficients in Fig. 17(d) show less improvement than expected from the simulations, and this is likely due to the inaccuracy of the made copper taped decoupling poles. From the measured reflections, (c), the measured impedance bandwidth again must be couched as a −5dB match, rather than a −10dB match. This is the same situation as in other mmWave antennas, e.g., [23].

Fig. 18 shows some simulated pattern cuts for the original design, and recall this is for the *unused elements terminated*, so the mutual coupling impacts the situation. At 25 GHz

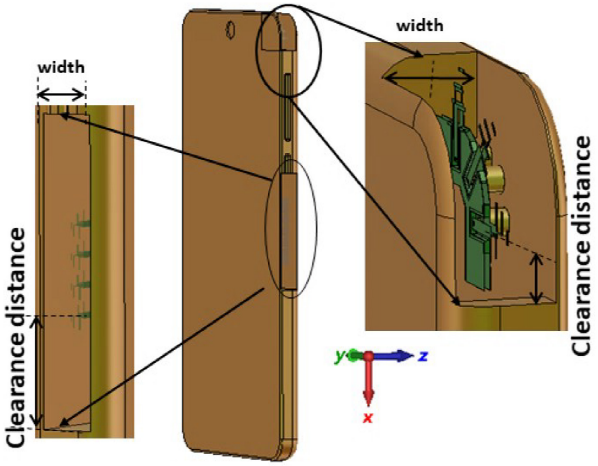

FIGURE 19. Deploying the linear array on the long side of a cellphone chassis, and the arc shaped array at a corner. Finite, complex platforms, such as these configurations affect array performance.

(28 GHz), ports 1 and 3 have a peak gain of 5.4 dBi (6.7 dBi) and port 2 (the middle element) is about 6 dBi (7.1 dBi). At higher frequencies, the gain increases because of the higher element directivity. For example at 40 GHz, ports 1 and 3 have a peak gain of 7.7 dBi and for port 2, 9.2 dBi.

For the *unused elements open circuited* (not shown), there is a gain increase at port 2 at 25 GHz of about 0.5 dB, and at 28 GHz, about 0.2 dB, and negligible change at 40 GHz. These differences are from the mutual coupling creating loss in the terminated unused ports.

For the improved design in the corner array (not shown), the lower mutual coupling at lower frequencies means that the beam direction becomes better aligned with the geometric steering direction and has improved gain. In particular, at 25 GHz the Port 1 peak gain is improved by 0.6 dB to 6.03 dB, from a narrowed E-plane (x-y) beamwidth but unchanged H-plane (x-z) pattern cut. For Port 2, the peak gain is improved by 0.4 dB. For port 3, the peak gain is again improved by 0.6 dB, similar to Port 1. At 28 GHz, similar but smaller changes occur, and once the frequency reaches 40 GHz, the mutual coupling is not changed and so the respective patterns are the same.

V. CHASSIS EFFECTS ON ARRAY

Examples of placing the arrays on a cell phone chassis are shown in Fig. 19. A cavity, i.e., an open-ended waveguide, is used for the antennas so that the antenna PCB structure is unobtrusive. A radome would be used over the cavity opening of the antenna system. We have not studied the impact of the radome. Generally, a low loss radome of modest relative permittivity, and electrically very thin, will not have a major impact. However, the complex chassis will impact the antenna. The size of the cavity is of primary interest, and we simulate a couple of options to identify a design, and its impact on the array performance.

A. LINEAR ARRAY

Chassis 1: The cavity width (between the parallel plates, see the left-most diagram of Fig. 19) is set to 8 mm, with cavity length 52 mm. Both ends of the cavity are 18.5 mm away from the center of the outer element of the array in the E-plane, depicted as "clearance distance" in Fig. 19. In the H-plane, the clearances to the cavity edges are 4.5 mm and 3 mm, i.e., the PCB antenna is not quite at the centre between the parallel plates. This is to cater for the antenna connectors which are on one side of the PCB. This is the widest cavity for the chassis, and we study the impact of reducing it.

Chassis 2: The cavity width is reduced from 8 mm to 6 mm, keeping the other clearances the same.

Chassis 3: the cavity size along E-plane is reduced so that clearance distance is reduced from 18.5 mm to 7.5 mm.

Fig. 20 shows the S-parameters of the linear array in the various chassis cavities. For the original design, some resonance-like behaviour of the cavity causes the reflection coefficients to increase - for example, going above −10 dB, and thereby disrupting the −10 dB bandwidth.

When the chassis cavity width is reduced, or the clearance distance is reduced, as in *Chassis 2* and *3*, respectively, the coupling between adjacent elements and the next-to-adjacent elements, are significantly affected. It seems that the narrower cavity width couples more energy between the ports from increased wave guiding within the cavity. This increased coupling in turn limits the scan range of beam steering arrays at lower frequencies. Of particular interest is that the original design is more sensitive to the cavity presence than the improved design. The improved design has lower coupling between elements, and this makes it more robust to cavity coupling-induced scan losses. The improved design operating in *Chassis 1* works satisfactorily in terms of reflection coefficients and coupling over the operating bandwidth, despite the cavity resonances.

This simulation study shows that the minimum cavity size should be *Chassis 1*, corresponding to 0.6 λ_0 and 3.8 λ_0 at the lowest frequency, 22 GHz. A smaller cavity size further compromises the bandwidth performance.

Table 2 summarizes the impact of the cavity presence on gain and beamwidth. For *Chassis 1*, at the low frequencies, the array directivity is increased significantly (by 3 dB) because the cavity acts to reduce the beamwidth. For the much-reduced cavity size of *Chassis 3*, the E-plane maintains the increased peak gain at the low bands, but by 40 GHz, the peak gain drops slightly. Table 3 gives the scan range performance in *Chassis 1*. The scan range of the original array is significantly reduced as a result of the chassis, mainly because of the reduced adjacent element coupling at lower frequencies. For the improved array inside the chassis cavity, the lower coupling means better scan range as seen in Table 3. Regarding the patterns, Fig. 21 shows the original array has scan range degradation for beam steering to 45° at 25 GHz, but remains good over its designed 3 dB scan range at 28 GHz and 40 GHz.

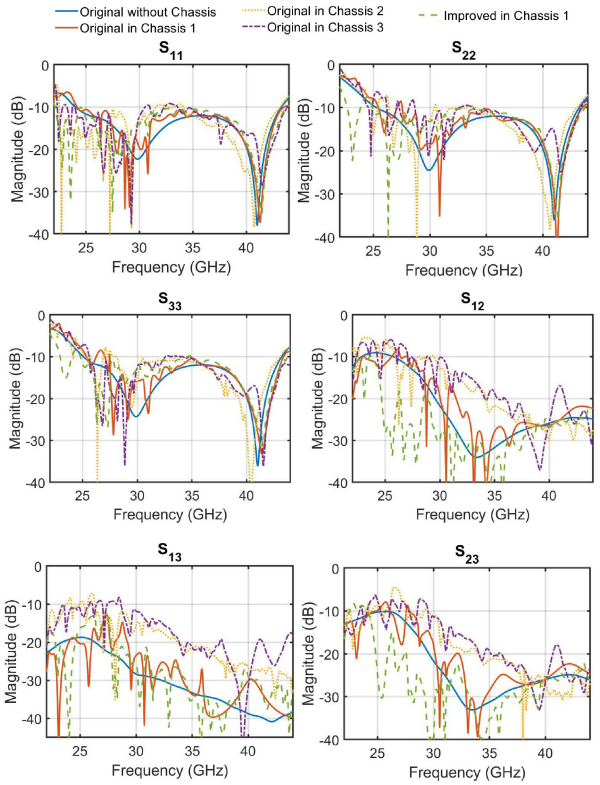

FIGURE 20. Simulated scattering parameters of original and improved design inside chassis cavity. The cavity resonance modes increase the coupling between the elements, and reduce the impedance bandwidth, when the enclosing cavity size becomes critically small.

TABLE 2. Gain and beamwidth comparisons for various cavity shapes for the linear array (original design) in the cellphone chassis.

Chassis size	Peak gain (dBi)	3 dB beamwidth H-Plane (deg)	3 dB beamwidth E-Plane (deg)
25 GHz			
None	9	158	27.3
Chassis 1	12.1	70.4	29
Chassis 2	11.5	88	22.7
Chassis 3	12.4	84	21.1
28 GHz			
None	9.7	140	24.5
Chassis 1	13.1	64	26
Chassis 2	12	95	18.4
Chassis 3	12.8	81.3	21.5
40 GHz			
None	13	97	18.8
Chassis 1	15	56	18.2
Chassis 2	14.6	65	18.3
Chassis 3	14.4	65.4	19.2

B. 3-ELEMENT CORNER ARRAY

The beam switched corner array is shown on the right hand side of Fig. 19, with the elements in a corner cavity of the chassis. Again, we experiment with the cavity size to see how it affects the array performance.

TABLE 3. Peak gain and scan range comparison of original and improved design of the linear array in *Chassis 1*.

Freq	Original		Improved	
-	Gain	Scan range	Gain	Scan range
GHz	dBi	3 dB	dBi	3dB
25	12.1	+20° to -42°	12.7	+37° to -38°
28	13.1	+41° to -46°	13.1	+45° to -48°
40	15	+38° to -19°	14.9	+38° to -18°

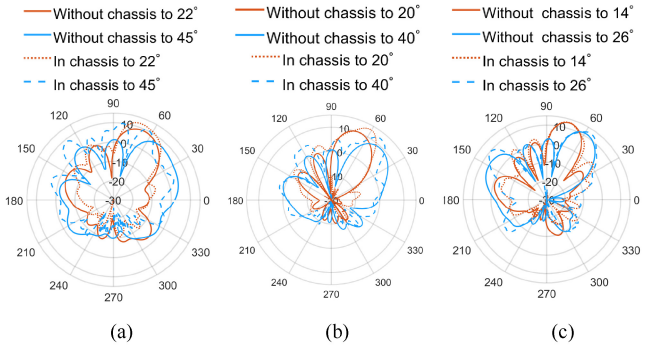

FIGURE 21. Simulations of the linear array to show the effect of the chassis mounting of the array on its beam steering for the original array at (a) 25 GHz (b) 28 GHz and (c) 40 GHz. The chassis acts to increase the gain of the array gain but reduces the scan range.

Corner Chassis 1: A cavity of 8 mm wide with E-plane clearance 8 mm (Fig. 19). The array, on 0.5 mm thick AiP, is symmetrically placed inside cavity with the cavity end walls at 3.8 mm on one side and 3.7 mm on other.

Corner Chassis 2: Cavity width reduced to 6 mm in the H-plane, maintaining the E-plane cavity edge wall at 8 mm away from centre of the port 1 element.

Corner Chassis 3: The whole cellphone chassis as a hollow enclosure between 1.5 mm thick copper parallel sheets, with a cutout clearance of 8 mm in the E-plane and a cavity width of 8 mm in the H-plane as in *Corner Chassis 1*.

The summary is as follows (plots of the details are omitted). *Corner Chassis 1* has negligible impact on impedance bandwidth and port isolation. The narrower cavity width of *Corner Chassis 2* affects all the reflection coefficients and reduces the −10 dB impedance bandwidth. The large cavity of *Corner Chassis 3* gives the same results as *Chassis 1*. From these results, the size of the clearances is the critical design parameter. So the *Corner Chassis 1* is the best choice, and with the improved design, the elements maintain their impedance bandwidth (22-43.5 GHz). To see the impact of the critically lower mutual coupling, the original design in the *Corner Chassis 1* cavity, has bandwidth (25-43.5 GHz), and the gain performance is about the same.

Table 4 reviews the impact of the various cavity sizes on the element gains. The end elements (ports 1 and 3) have slightly different gains, which is due to the asymmetric PCB layout of the elements and their slightly different (3.7 mm and 3.8 mm) wall clearances. The presence of the chassis can improve the gain for all ports by 2 to 3 dB.

TABLE 4. Gain (dBi) comparisons for the various cavities of the corner array for the beam switching array.

Cavity type	Port 1	Port 2	Port 3
25 GHz			
Original without chassis	5.45	6.07	5.35
Original with Corner chassis 1	8.22	8.25	7.2
Original with Corner chassis 2	8.87	7.56	7.37
Original with Corner chassis 3	8.08	8.28	7.32
Improved without chassis	6.03	6.31	6.01
Improved with Corner chassis 1	8.16	7.96	8.14
28 GHz			
Original without chassis	6.72	7.11	6.6
Original with Corner chassis 1	8.82	8.92	7.88
Original with Corner chassis 2	9.13	8.84	8.28
Original with Corner chassis 3	9.16	8.95	7.47
Improved without chassis	6.41	6.9	6.25
Improved with Corner chassis 1	8.91	8.53	8.1
40 GHz			
Original without chassis	7.75	9.21	7.63
Original with Corner chassis 1	9.99	10.7	8.98
Original with Corner chassis 2	9.43	10.3	8.62
Original with Corner chassis 3	9.66	10.7	8.81
Improved without chassis	7.53	9.09	7.4
Improved with Corner chassis 1	9.84	10.9	9.04

In summary, the cavity width (relates to the thickness of the cellphone chassis) for these elements should be 8mm, corresponding to 0.6 λ_0, with an E-plane clearance of 0.6λ_0 at 22 GHz (lowest operating frequency) to minimize the impact on the port impedances.

VI. CONCLUSION

Design information is presented for a new element and its arrays which are suitable for cellphones operating over a set of 5G frequency bands. The designs use Antenna-in-Package technology including substrates of Liquid Crystal Polymer for its stable dielectric constant. An "original" design is compared with an "improved" design which has decreased mutual coupling from using a known decoupling modification. The impact of the associated critical change in mutual coupling is presented in terms of the array performance. The element has a 66% relative impedance bandwidth. For the arrays, the lowest frequencies have the smallest electrical spacing where the mutual coupling limits the gain, while at the highest frequencies, the large electrical spacing causes grating lobes. These opposing effects are traded off using a design approach which depends on both the array factor and the element pattern. The result is a better scan range across the wide bandwidth than that available from the traditional formulation which uses only the array factor. At 25 GHz (the lowest 3GPP-tagged mmWave band), the adjacent element mutual coupling is improved from −10 to −20 dB. For a linear array this extends the TARC bandwidth of the array in the lower frequency direction by 5GHz. This also increases: the 3dB scan range by 30°; the broadside array antenna gain by 0.8dB (and by more in off-broadside directions); and the array antenna radiation efficiency by 0.4 dB. For the 28 GHz band, the adjacent element coupling level decreases from −15 to −25 dB, which increases: the array antenna 3 dB scan range by 17°; the broadside array antenna gain by 0.6 dB; and the radiation efficiency by 0.2 dB. At higher frequencies, where the electrical spacing is larger, the mutual coupling is about −25 dB, a level which is low enough to have negligible impact on the phased array performance.

Deploying the array on a mobile terminal changes the array performance relative to its stand-alone behaviour. It was shown by simulation that placing the array in a cavity of a cellphone chassis reduces the beamwidth and boosts the peak gain by 2-3 dB. In reducing the beamwidth, the 3 dB scan range is reduced: by 30°, 29°, and 19°; at 25 GHz, 28 GHz and 40 GHz, respectively. To maintain the bandwidth of the array in the chassis, we established a minimum cavity clearance for the antenna (see Fig. 19) in both the E-plane and the H-plane of the array.

TABLE 5. Comparison of presented array antenna with recently published mmWave array antennas.

Design	Bandwidth GHz	Array Gain dBi	3 dB Scan Range	Pol
This paper	24-44 (59%)	9.8-13.6	± 60° - ± 35°	Single
[9], (2022)	24.5-29.5 (19%)	10-11	± 50°	Dual
[15], (2017)	24-32 (29%)	8.2–9.6	± 35°	Single
[12], (2017)	31-40 (25%)	11	NA	Dual
[13], (2019)	25-30 (18%)	8-10	NA	Single

APPENDIX
SUMMARY OF REPRESENTATIVE PUBLISHED MMWAVE ARRAYS

With our design results in place, the performance of our improved linear array can be compared to recently published wideband mmWave arrays antennas (with no chassis included). Table 5 is the summary showing a favourable comparison in the gain and bandwidth.

REFERENCES

[1] "FCC establishes procedures for first 5G spectrum auctions." Federal Communication Commission. 2018. [Online]. Available: https://www.fcc.gov/document/fcc-establishes-procedures-first-5g-spectrum-auctions-0

[2] W. Hong et al., "Multibeam antenna technologies for 5G wireless communications," *IEEE Trans. Antennas Propag.*, vol. 65, no. 12, pp. 6231–6249, Dec. 2017.

[3] R. Méndez-Rial, C. Rusu, N. González-Prelcic, A. Alkhateeb, and R. W. Heath, "Hybrid MIMO architectures for millimeter wave communications: Phase shifters or switches?" *IEEE Access*, vol. 4, pp. 247–267, 2016.

[4] A. C. K. Mak, C. R. Rowell, and R. D. Murch, "Isolation enhancement between two closely packed antennas," *IEEE Trans. Antennas Propag.*, vol. 56, no. 11, pp. 3411–3419, Nov. 2008.

[5] T. S. Bird, *Mutual Coupling Between Antennas*. Hoboken, NJ, USA: Wiley, 2021.

[6] M. Razmhosseini, A. Bhattacharya, and R. G. Vaughan, "Practical diversity design for PCB IoT terminals," *IEEE Open J. Antennas Propag.*, vol. 1, pp. 627–643, 2020.

[7] P. Liu, X.-W. Zhu, Y. Zhang, X. Wang, C. Yang, and Z. H. Jiang, "Patch antenna loaded with paired shorting pins and H-shaped slot for 28/38 GHz dual-band MIMO applications," *IEEE Access*, vol. 8, pp. 23705–23712, 2020.
[8] M. Sun, X. Qing, and Z. N. Chen, "60-GHz end-fire fan-like antennas with wide beamwidth," *IEEE Trans. Antennas Propag.*, vol. 61, no. 4, pp. 1616–1622, Apr. 2013.
[9] L. Sun, Y. Li, and Z. Zhang, "Wideband dual-polarized endfire antenna based on compact open-ended cavity for 5G mm-Wave mobile phones," *IEEE Trans. Antennas Propag.*, vol. 70, no. 3, pp. 1632–1642, Mar. 2022.
[10] N. Kaneda, W. Deal, Y. Qian, R. Waterhouse, and T. Itoh, "A broadband planar quasi-Yagi antenna," *IEEE Trans. Antennas Propag.*, vol. 50, no. 8, pp. 1158–1160, Aug. 2002.
[11] D. Wang et al., "A planar quasi Yagi-Uda antenna designed for liquid crystal based end-fire phased arrays," in *Proc. IEEE Radio Wireless Symp. (RWS)*, 2021, pp. 164–167.
[12] Y.-W. Hsu, T.-C. Huang, H.-S. Lin, and Y.-C. Lin, "Dual-polarized quasi Yagi–Uda antennas with endfire radiation for millimeter-wave MIMO terminals," *IEEE Trans. Antennas Propag.*, vol. 65, no. 12, pp. 6282–6289, Dec. 2017.
[13] I.-J. Hwang, B. Ahn, S.-C. Chae, J.-W. Yu, and W.-W. Lee, "Quasi-Yagi antenna array with modified folded dipole driver for mmWave 5G cellular devices," *IEEE Antennas Wireless Propag. Lett.*, vol. 18, no. 5, pp. 971–975, May 2019.
[14] Y. Li and K.-M. Luk, "A multibeam end-fire magnetoelectric dipole antenna array for millimeter-wave applications," *IEEE Trans. Antennas Propag.*, vol. 64, no. 7, pp. 2894–2904, Jul. 2016.
[15] B. Yang, Z. Yu, Y. Dong, J. Zhou, and W. Hong, "Compact tapered slot antenna array for 5G millimeter-wave massive MIMO systems," *IEEE Trans. Antennas Propag.*, vol. 65, no. 12, pp. 6721–6727, Dec. 2017.
[16] Y. Hu et al., "A digital multibeam array with wide scanning angle and enhanced beam gain for millimeter-wave massive MIMO applications," *IEEE Trans. Antennas Propag.*, vol. 66, no. 11, pp. 5827–5837, Nov. 2018.
[17] B. Yu, K. Yang, C.-Y.-D. Sim, and G. Yang, "A novel 28 GHz beam steering array for 5G mobile device with metallic casing application," *IEEE Trans. Antennas Propag.*, vol. 66, no. 1, pp. 462–466, Jan. 2018.
[18] S. Zhang, I. Syrytsin, and G. F. Pedersen, "Compact beam-steerable antenna array with two passive parasitic elements for 5G mobile terminals at 28 GHz," *IEEE Trans. Antennas Propag.*, vol. 66, no. 10, pp. 5193–5203, Oct. 2018.
[19] C. E. Patterson, W. T. Khan, G. E. Ponchak, G. S. May, and J. Papapolymerou, "A 60-GHz active receiving switched-beam antenna array with integrated butler matrix and GaAs amplifiers," *IEEE Trans. Microw. Theory Techn.*, vol. 60, no. 11, pp. 3599–3607, Nov. 2012.
[20] W. T. Khan, A. L. V. López, A. A. Ulusoy, and J. Papapolymerou, "Packaging a W-band integrated module with an optimized flip-chip interconnect on an organic substrate," *IEEE Trans. Microw. Theory Techn.*, vol. 62, no. 1, pp. 64–72, Jan. 2014.
[21] S. Pinel, I. K. Kim, K. Yang, and J. Laskar, "60 GHz linearly and circularly polarized antenna arrays on liquid crystal polymer substrate," in *Proc. Eur. Microw. Conf.*, 2006, pp. 858–861.
[22] H.-L. Kao et al., "Bending effect of an inkjet-printed series-fed two-dipole antenna on a liquid crystal polymer substrate," *IEEE Antennas Wireless Propag. Lett.*, vol. 13, pp. 1172–1175, 2014.
[23] C. Di Paola, S. Zhang, K. Zhao, Z. Ying, T. Bolin, and G. F. Pedersen, "Wideband beam-switchable 28 GHz quasi-Yagi array for mobile devices," *IEEE Trans. Antennas Propag.*, vol. 67, no. 11, pp. 6870–6882, Nov. 2019.
[24] R. S. Brar, R. G. Vaughan, and M. Felipe, "Phased arrays and MIMO: Wideband 5G end fire elements on liquid crystal polymer for MIMO," in *Proc. IEEE Int. Symp. Phased Array System Technol. (PAST)*, 2019, pp. 1–5.
[25] "LCP datasheet." Panasonic. 2021. [Online]. Available: https://industrial.panasonic.com/content/data/EM/PDF/emscatalog_felioslcp.pdf
[26] H.-C. Huang, J.-C. Lu, and P. Hsu, "A compact dual-band printed Yagi-Uda antenna for GNSS and CMMB applications," *IEEE Trans. Antennas Propag.*, vol. 63, no. 5, pp. 2342–2348, May 2015.
[27] R. Mailloux, "Array characterization for radar and communication system," in *Phased Array Antenna Handbook*. Norwood, MA, USA: Artech House, 2017, pp. 26–28.
[28] Y. Qian, W. Deal, N. Kaneda, and T. Itoh, "Mutual coupling and mitigation in two-dimensional phased arrays based on planar quasi-Yagi antennas," in *Proc. Asia-Pacific Microw. Conf.*, 2000, pp. 5–8.
[29] D. Pozar, "A relation between the active input impedance and the active element pattern of a phased array," *IEEE Trans. Antennas Propag.*, vol. 51, no. 9, pp. 2486–2489, Sep. 2003.
[30] B. A. Arand, A. Bazrkar, and A. Zahedi, "Design of a phased array in triangular grid with an efficient matching network and reduced mutual coupling for wide-angle scanning," *IEEE Trans. Antennas Propag.*, vol. 65, no. 6, pp. 2983–2991, Jun. 2017.
[31] H. Abdallah and W. Wasylkiwskyj, "A numerical technique for calculating mutual impedance and element patterns of antenna arrays based on the characteristics of an isolated element," *IEEE Trans. Antennas Propag.*, vol. 53, no. 10, pp. 3293–3299, Oct. 2005.
[32] R. S. Brar and R. G. Vaughan, "Dual-slot cavity antenna for mm-Wave beamforming array," *IEEE Access*, vol. 10, pp. 97047–97060, 2022.
[33] M. Manteghi and Y. Rahmat-Samii, "Multiport characteristics of a wide-band cavity backed annular patch antenna for multipolarization operations," *IEEE Trans. Antennas Propag.*, vol. 53, no. 1, pp. 466–474, Jan. 2005.

RAJVEER S. BRAR (Graduate Student Member, IEEE) received the B.Tech. degree in electronics and communication engineering from Guru Nanak Dev University, Amritsar, India, in 2013, and the M.Tech. degree in electronics engineering from the Indian Institute of Technology (BHU) Varanasi, Varanasi, India, in 2015. He is currently pursuing the Ph.D. degree in engineering science with Simon Fraser University, Burnaby, BC, Canada.

From 2015 to 2016, he was a Project Engineer with the Metamaterials Lab, Department of Electrical Engineering, Indian institute of Technology Kanpur, Kanpur, India, where he designed multi-polarization multi-band antennas for communication systems. He Interned with Benchmark Electronics, Phoenix, AZ, USA, from 2018 to 2019, and Qualcomm Inc., San Diego, CA, USA, in 2021. His research interests include the development of phased array antennas, multiple antennas for MIMO, reflecting surfaces for 5G, and mmWave antennas.

RODNEY G. VAUGHAN (Life Fellow, IEEE) is the Sierra Wireless Professor of Communications with the Department of Engineering Science, Simon Fraser University, Burnaby, BC, Canada. His university training was in New Zealand and Denmark. Most of his career has involved industrial development, where the value of research ultimately drew him to academia. His research revolves around information channels and the interplay between communications techniques, signal processing, and the physical aspects-the sensors, and the propagation and scattering of fields and waves. His current projects include the theory, design, and evaluation methods for adaptive antenna systems and adaptive acoustic systems. He is a Professional Engineer registered in BC, Canada, a 2004 Fellow of the BC Advanced System Institute, a Senior Member of URSI and continues as the New Zealand URSI Commission B Representative. He has had Chair roles for IEEE conferences. In 2006, he has served on the International Panel for Reviewing the Funding and Knowledge Base for Information and Communications Technology in the U.K., and in 2011 for the Communications Research Centre, Canada, and for the ICT Centre of the CSIRO, Australia. He has guest-edited Special Issues and has been an Associate Editor of the IEEE TRANSACTIONS ON ANTENNAS AND PROPAGATION. He was a IEEE Distinguished Lecturer of the Vehicular Technology Society from 2012 to 2018.